Prediction of the spreading of an unprecedented Karenia mikimotoi bloom in South Australian gulfs

Preprint · July 2025

DOI: 10.13140/RG.2.2.28102.59207

1 author:

Jochen Kaempf
Flinders University
110 PUBLICATIONS **2,267** CITATIONS

SEE PROFILE

Manuscript submitted to Continental Shelf Research 18 July 2025

Prediction of the spreading of an unprecedented *Karenia mikimotoi* bloom in South Australian gulfs

Jochen Kämpf

College of Science & Engineering, Flinders University, Adelaide, Australia

Corresponding author: jochen.kaempf@flinders.edu.au

Abstract: Using a coupled physical-biological model, this work aims to predict the spreading of an unprecedented *Karenia mikimotoi* bloom that since March 2025 has caused kills of crustacean, fish and other marine life in Gulf St. Vincent, which alongside Spencer Gulf is one of the two South Australian gulfs. The gulfs are large inverse estuaries with limited physical connectivity with the ambient coastal ocean. The model simulations confirm that timeline of the initial bloom spreading, which started in mid-March 2025 just outside Gulf St. Vincent, then was brought into the lower gulf via tidal stirring in Backstairs Passage, before it spread clockwise around Gulf St. Vincent with the prevailing density-driven circulation, all in the matter of 2-3 months. While the seasonal cooling of gulf water will naturally reduce algae growth over winter months, the simulations show that the possible reactivation of algae growth in future summers strongly depends on the zooplankton grazing rate, assumed constant in the model. The worst-case scenario predicts spreading of *Karenia mikimotoi* blooms into the Spencer Gulf where it could cause severe damage to the existing large stocks of Australian sardine (*Sardinops sagax*), western king prawn (*Penaeus latisulcatus*) and the Giant Australian Cuttlefish (*Sepia apama*). Discussed is also the suitability of satellite-derived chlorophyll-*a* data to track the algae bloom.

Key words: Harmful algae bloom; Karenia mikimotoi; Inverse estuaries; Physical-Biological Interactions; Computer modelling

Highlights:

- An unprecedented *Karenia mikimotoi* bloom has evolved in South Australian gulfs since mid-March 2025
- A coupled physical-biological model is used to predict the spreading of this bloom
- The model largely reproduces the reported initial spreading of the bloom
- The future reactivation of *K. mikimotoi* blooms in the gulfs depends strongly on the degree of zooplankton grazing

1. Introduction

Harmful Algae Blooms (HABs) are events in which the growth of marine algae lead to damage of marine ecosystems including mortality of fish and shellfish affecting human health (Glibert and Pitcher, 2001). More than 200 species of algae, ranging in size from pico-to mega-algae, can form HABs (Sournia, 1995). Increasing numbers of toxic dinoflagellate blooms have been recorded in recent decades (Furuya et al., 2018; Glibert et al., 2018).

Karenia mikimotoi (henceforth *K. mikimotoi*) is a bloom-forming dinoflagellate in the genus *Karenia*. Blooms of this algae, observed since the 1930s, have caused mass mortalities of fish, shellfish, and other invertebrates in coastal oceans worldwide for many decades and preceding the era of accelerating climate change. See Li et al. (2019) for a comprehensive review of major *K. mikimotoi* events that are characterized by concentrations of 10^3-10^5 cells ^{per} mL. Blooms cause significant gill disorder in affected fish, which can lead to massive fish kills, rather than hypoxia that may occur in the fading stage of a bloom (Li et al., 2019). Previous research suggested that grazing by zooplankton may play a central role in the bloom decay stage of *K. mikimotoi*. For instance, the heterotrophic dinoflagellates (*Gyrodinium dominans* and *Gyrodinium spirale*) and tintinnid ciliate (*Favella ehrenbergii*) were observed increased during decay stage of *K. mikimotoi* in the Seto Inland Sea, Japan (Nakamura et al., 1996, 1995).

There are several modelling studies attempting to simulate blooms of *K. mikimotoi* with coupled physical-biological models. This includes the modelling study by Vanhoutte-Brunier et al. (2008) of a large *K. mikimotoi* bloom that occurred in the English Channel during summer 2003, modelling of *Gymnodinium mikimotoi* blooms along the French Atlantic coast by Loyer et al. (2001), and individual-based modelling of the development and transport of a *K. mikimotoi* bloom on the North-west European continental shelf by Gillibrand et al. (2016). These studies form the theoretical background for the *K. mikimotoi* model used in this paper.

This study focusses on South Australian gulfs, Spencer Gulf and Gulf St Vincent (**Figure 1**). The southern continental shelf of Australia (which includes South Australian gulfs) hosts a large seasonal coastal upwelling system (Kämpf et al., 2005), known as Great Southern Australian Coastal Upwelling System (GSACUS) (Kämpf, 2024, 2025a,b). High abundances of Australian sardine (*Sardinops sagax*) and anchovy (*Engraulis australis*) are the keystone forage fish of this upwelling system providing the diet for a range of predators including

southern bluefin tuna (*Thunnus maccoyii*), sea lions, seals, sharks and seabirds (Ward et al., 2006, noting the existence of a significant sardine stock near and in the lower Spencer Gulf.

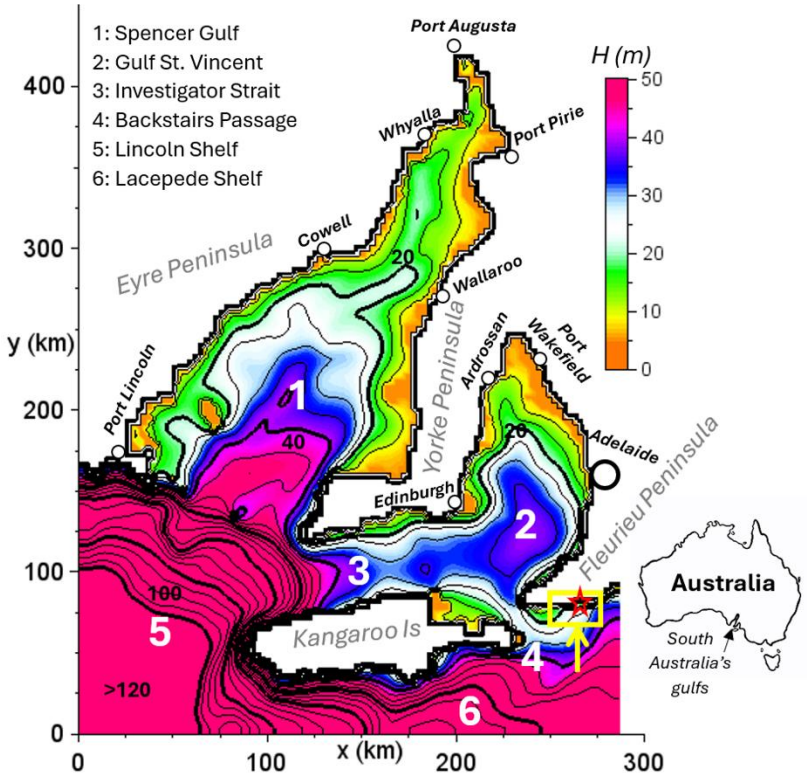

Figure 1: Bathymetry (m) of the model domain (color shading and lines; CI = 5 m; thick lines are shown with CI = 20 m). The Australia map shows the location of South Australia's gulfs. The yellow rectangle shows the algae release region. The red star shows the location of Waitpinga Beach where the toxic algae was first identified. Data source: Geoscience Australia.

Three distinct blooms of *K. mikimotoi* have been previously reported near South Australian gulfs, Spencer Gulf and Gulf St. Vincent. Two events occurred in Coffin Bay, which is a small inter-tidal estuary located a short distance (~50 km) west from the mouth of Spencer Gulf (Kämpf and Ellis, 2015). In March 1995, *K. mikimotoi* was attributed to a multi-species kill in in this estuary with abalone, cockles, stingrays and multiple fish species being affected (Gaut, 2001). A similar event developed in Coffin Bay in February 2024 (Roberts et al., 2014) with peak cell counts of 1.6×10^4 cells ml^{-1}. Both events remained localized within the Coffin Bay estuary and did not affect the wider upwelling ecosystem. A recent study (Kämpf, 2025c) confirms a limited connectivity between the upwelling plume and the inner bays of the Coffin Bay estuary. The third *K. mikimotoi* bloom developed

recently in mid-March 2025 in bays on the southern coastline of the Fleurieu Peninsula just outside Backstairs Passage (**Figure 2**).

Figure 2: Sea foam produced by the *K. mikimotoi* bloom at Waitpinga Beach on the southern headland of the Fleurieu Peninsula) in mid-March 2025. Image credit: Caroline Horn (ABC). Reproduced with permission.

Both South Australian gulfs are shallow bodies of water less than 50 m deep (see Figure 1). Spencer Gulf is the larger of the two gulfs being bordered by Eyre Peninsula in the west and Yorke Peninsula in the east. It is a triangular-shaped embayment, 300 km long, with a mean depth of 24 m. Spencer Gulf is divided into a deeper and wider southern area and a much narrower and shallower northern area, called Upper Spencer Gulf. The latter features the world's only know mass spawning aggregation of the Giant Australian Cuttlefish (*Sepia apama*) (Dupavillon and Gillanders 2009), and the world's largest population of the western king prawn (*Penaeus latisulcatus*) (Richardson 1982).

Gulf St. Vincent is bordered by York Peninsula in the west and Fleurieu Peninsula in the east. Whereas Spencer Gulf has only one entrance, Gulf St. Vincent is connected to the adjacent coastal ocean via two entrances, Investigator Strait, about 30–45 km wide and with a mean depth of 34 m, and Backstairs Passage, only 14 km wide. Investigator Strait is bordered by Kangaroo Island in the south. Gulf St. Vincent and Investigator Strait together are 210 km in length. Gulf St. Vincent has a mean depth of 20 m and features a 40-m deep basin in its southern part. Backstairs Passage has a sill where total water depth reduces to ~35 m.

Both gulfs are exposed to a semi-arid temperate climate with annual evaporation (~2 m) exceeding precipitation (~45 cm) by far (Kämpf, 2014). Together with low river runoff, the

regional climate makes both gulfs hypersaline inverse estuaries. The seasonal climate is a Mediterranean type with dry summers and wet winters. Seasonal cooling of hypersaline gulf waters induces a density-driven exchange circulation between the gulfs and the ambient continental shelf in late austral winter and spring (Lennon et al., 1987; Kämpf et al. 2009). This overturning circulation constitutes the only means of flushing of the gulfs. It ceases during summer when warming of the water column reduces the relative density excess in gulf waters (Kämpf et al., 2009).

The tides in Gulf St. Vincent are predominantly semidiurnal with modulations by diurnal tidal constituents (K1 and O1). In Spencer Gulf, the tidal signal is mixed semi-diurnal/diurnal as the amplitude of the K1 is close to that of the semidiurnal tides. The closeness of the amplitudes of the S2 and M2 in both gulfs leads to an almost vanishing neap tide, known as dodge tide. Moreover, resonance of the semidiurnal tides leads to an amplification of the tidal ranges (and tidal currents) in the upper reaches of both gulfs, with a tidal range >4m in Upper Spencer Gulf. A slightly lower tidal range of 3 m occurs during spring tides near the head of Gulf St. Vincent. Backstairs Passage features strong tidal flows >1 m/s during spring tides.

The following reconstructed timeline of the spreading of the *K. mikimotoi* bloom serves as a reference for the validation of the model predictions presented in this paper. According to the Environment Protection Authority of South Australia (EPA, 2025) the *K. mikimotoi* bloom developed in mid-March 2025 in the waters of Waitpinga Beach and Parsons Beach on the southern headland of the Fleurieu Peninsula; that is, outside South Australian gulfs (see Figure 1). In mid-April, the bloom was detected in water samples collected from Edithburgh and Coobowie located on the southeastern corner of the Yorke Peninsula (Daw, 2025). At this time *K. mikimotoi* was not detected at other sample locations along the shores of Gulf St Vincent. In early May, the Kangaroo Island Council (Kangaroo Island Council, 2025) stated that the bloom has spread across the Investigator Strait affecting the Kangaroo Island coastline. Eventually, in early July, the South Australian Government has confirmed the detection of *K. mikimotoi* along Adelaide's metropolitan coastline (Government of South Australia, 2025), around 4.5 months after its first detection outside South Australian Gulfs. Videos of fish kills near the Ardrossan Jetty in the northern Gulf St. Vincent (see Figure 1) appeared in early July. So far, toxic algae have not been detected in Spencer Gulf. Citizen science projects have been established to archive and track the environmental damage due to the algae bloom using iNaturalist as a data platform.

2. Methodology

2.1 Hydrodynamic model

This work uses the sigma-coordinate hydrodynamic model COHERENS (Luyten et al., 1999). Kämpf et al. (2009) previously calibrated this model for the South Australian Gulfs with a focus on an accurate simulation of both tides and the seasonal temperature and salinity cycles within both gulfs.

The model domain is discretized in a with 10 equidistant sigma layers and horizontal grid spacings of $\Delta x = 2.73$ km in the zonal direction and previously calibrated by $y = 3.33$ km in the meridional direction. See Kämpf et al. (2009) for a full model description. While retaining an accurate simulation of the gulfs' residual circulation, this relatively coarse grid resolution allows for total simulation times of 3-5 years with a numerical time step of $\Delta t = 30$ s within reasonable CPU times of 3-4 days.

The model is forced by surface winds and surface heat and freshwater fluxes based on monthly mean climatological data taken from the NCEP reanalysis grid for the period 1978–1998 and regional relative humidity data provided by the Australian Bureau of Meteorology. Tidal sea-level boundary forcing is implemented at the western and eastern open boundaries of the model domain using amplitudes and phases of the four dominant tidal constituents (M2, S2, O1 and K1) provided by the National Tidal Centre of the Bureau of Meteorology, Australia. Zero-gradient conditions are used for sea levels along the southern boundary. Along the open boundaries, a seasonal cycle of temperatures is prescribed while salinity is kept at a constant value.

A constant horizontal eddy viscosity of 5 $m^2 s^{-1}$ is used. A classical k-ε turbulence closure model with standard settings is used to calculate vertical eddy viscosity. Eddy diffusivities are computed from a turbulent Schmidt number of 0.8. Relatively accurate tidal predictions were achieved with the use of a quadratic bottom-friction parameterization with a spatially uniform bottom roughness length of 5 mm (see Kämpf et al., 2009).

2.2 The *Karenia mikimotoi* model

a. The complete model

The growth and dispersal of *K. mikimotoi* is predicted from an advection-diffusion equation formulated for an Eulerian tracer field, P, that including exponential growth and decay terms is given by:

$$\partial P/\partial t = \mathrm{adv}(P) + \mathrm{diff}(P) + \mu P - mP^2 - g_r P \quad (1)$$

where t is time, adv(.) and diff(.) are advection and diffusion operators, and μ, m and g_r are growth, mortality and grazing parameters, respectively. Locomotion by algae is ignored. Previous models of *K. mimimotoi* growth by Gentien et al. (2007), Vanhoutte-Brunier et al. (2008) and Gillibrand et al. (2016) did not account for the zooplankton grazing term. The advection and diffusion operators are defined (in Cartesian coordinates) by:

$$\mathrm{adv}(.) = -\left(u\frac{\partial}{\partial x} + v\frac{\partial}{\partial y} + w\frac{\partial}{\partial z}\right) \quad (2)$$

$$\mathrm{diff}(.) = \frac{\partial}{\partial x}\left(D_h\frac{\partial}{\partial x}\right) + \frac{\partial}{\partial y}\left(D_h\frac{\partial}{\partial y}\right) + \frac{\partial}{\partial z}\left(D_z\frac{\partial}{\partial z}\right) \quad (3)$$

where (u, v, w) is the velocity vector, and D_h and D_z are horizontal and vertical eddy diffusivities, simulated by the hydrodynamic model.

The growth rate μ is a function of temperature (T), salinity (S), light (L) and nutrients (N), which can be formulated as:

$$\mu = \mu_o(T,S)f(L)f(N) \quad (4)$$

where μ_o is the maximum growth rate under saturated light and nutrient conditions and $f(L)$ and $f(N)$ are limiting functions. The growth rate μ_o can be described by the equation (Nielsen and Tonseth, 1991):

$$\mu_o(T,S) = 0.15T + 0.15S - 0.004T^2 - 0.003S^2 + 0.001S \times T - 3.142 \quad (5)$$

The optimum ranges (capturing 10% of the highest growth rate) occur in the temperature and salinity ranges of 17.5–22.5°C and 24.5–34, respectively **(Figure 3)**. Note that, according to

(5), *K. mimimotoi* does neither grow in freshwater ($S < 14$ ppt), hypersaline ($S > 43$ ppt) nor cold-water environments ($T < 10$°C).

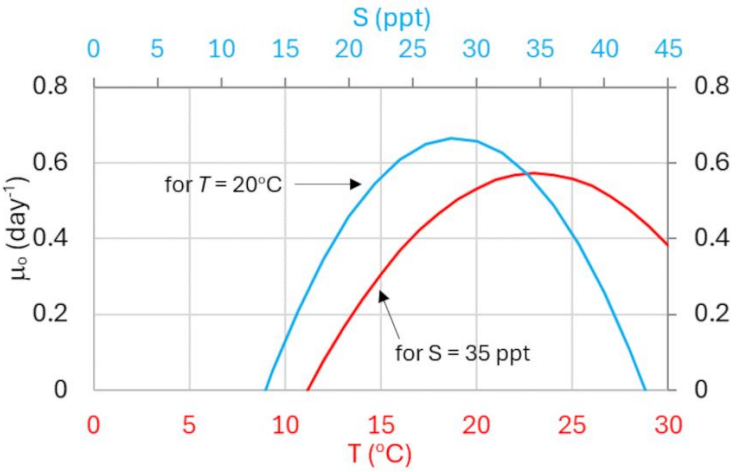

Figure 3: Projections of the maximum growth rate μ_o under saturated light and nutrient conditions for (blue curve) a constant temperature of $T = 20$°C and (red curve) a constant salinity of $S = 35$ ppt, calculated from (5).

Photosynthetically active radiation, I_z, is approximated by the classical exponential light-attenuation curve:

$$I_z(t,z) = I_o(t)e^{-a_w z} \tag{6}$$

where I_o is surface radiance, z is depth, and a_w is light attenuation coefficient, set to $a_w = 0.1$ m^{-1}. Effects due to self-shading by particles are ignored. Surface radiance is a function of the day-night sunlight cycle, which depends on location and time of year, and cloud coverage. For simplicity, this is expressed here by a simplified day-night cycle according to:

$$I_o(t) = \max[I_s(\mathrm{t})\sin(2\pi t/86400),0] \tag{7}$$

where I_s is the seasonal cycle of the daily maximum radiance, prescribed as:

$$I_s(t) = I_a + I_b\cos(2\pi\, month/12) \tag{8}$$

with $I_a = 400$ W m^{-2}, $I_b = 200$ W m^{-2}, and *month* referring to the month number. For simplicity, the seasonal variation of daylight duration is ignored. The daily average of (7) is given by I_s/π. The light-limiting function in (4) can then be formulated by a Michaelis-Menten type relationship; that is:

$$f(L) = I_z/(I_z + K_I) \tag{9}$$

where K_I = 1.15 W/m^2 is the half-saturation constant for irradiance, as also used in the study by Vanhoutte-Brunier et al. (2008). Note that K_I corresponds to a depth of ~52 m during summer and ~41 m in winter for the prescribed radiance variation. Hence, light does not limit the growth of *K. mimimotoi* in the shallow waters of South Australian gulfs in this model. Moreover, *K. mimimotoi* can grow at low nitrogen conditions and thrive mainly on ammonia (Vanhoutte-Brunier et al., 2008). Analog to (9) this can be expressed as:

$$f(N) = NH_4/(NH_4 + K_{NH_4}) \quad (10)$$

where K_{NH4} = 0.01 µmol l^{-1}. Field data for South Australian gulfs (Middleton et al., 2013) indicate that ammonia concentrations are commonly above the latter threshold. For this reason, this study assumes $f(N) = 1$, which implies that nutrients do not limit the growth *K. mimimotoi* in the gulfs.

The mortality rate m in (1) is formulated as (e.g., Gentien et al., 2007):

$$m = m_o \alpha \gamma \quad (11)$$

where m_o is a constant, γ is the shear rate (day^{-1}), and α describes additional physiological effects. The shear rate (in units of day^{-1}) is given by (Moum and Lueck,1985):

$$\gamma = 86400\sqrt{\epsilon/(7.5\,\nu)} \quad (12)$$

where ε is the dissipation rate (predicted by the hydrodynamic model) and ν = 10^{-6} m^2 s^{-1} is the kinematic molecular viscosity. Note that Vanhoutte-Brunier et al. (2008) formulate α in (11) as a function of temperature as:

$$\alpha(\mathrm{T}) = \min\{\max[(T - 15)/5{,}0] + 0.05{,}1\} \quad (13)$$

As demonstrated in the next section, this formulation leads to unrealistic algae growth and is therefore not implemented here. Instead, this study adopts α = 1 together with m_o = 5×10^{-5} (cells ^{per} L)$^{-1}$, as in Gentien et al. (2016) and Gillibrand et al. (2016). Note that Loyer (2001) used a larger value of m_o = 2.7×10^{-4} (cells ^{per} L)$^{-1}$. Values of the grazing rate g_r in (1), not used in previous studies, are varied in a sequence of sensitivity experiments.

b. Theoretical consideration

The following theoretical considerations help with the interpretation of the simulation results. Without mortality, grazing, and physical processes, equation (1) reduces to:

$$dP/dt = +\mu P \tag{14}$$

which has the analytical solution:

$$P(t) = P_o \exp(\mu t) \tag{15}$$

where P_o is the initial value. Here the concentration increases exponentially without bound (**Figure 4a**). When adding a mortality term with a constant m, the governing equation is given by:

$$dP/dt = +\mu P - mP^2 \tag{16}$$

which has the analytical solution:

$$P(t) = \mu[m + \kappa \exp(-\mu t)]^{-1} \text{ with } \kappa = \mu/P_o - m \tag{17}$$

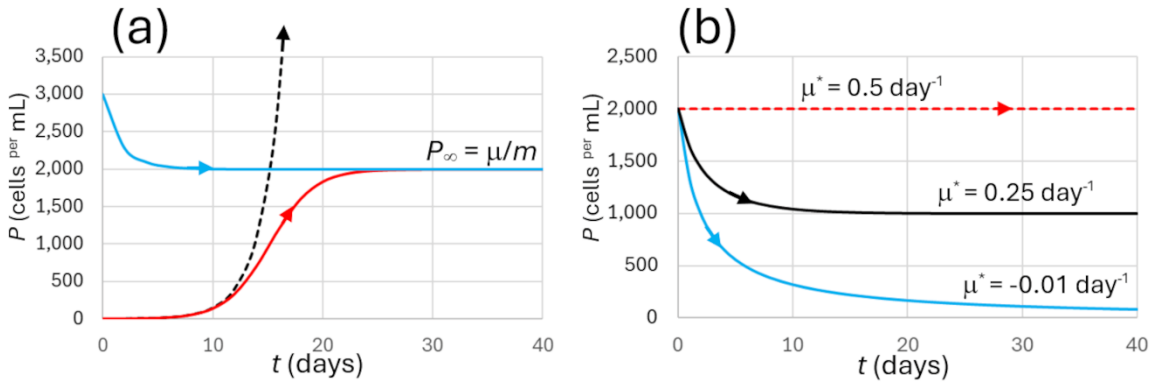

Figure 4: Analytical solutions for $\mu = 0.5$ day^{-1}. (a) The dashed black curve is the solution (15) for $P_o = 1$ cell ^{per} ml. The red curve is the corresponding solution (17) with $m = 7.5\times10^{-7}$ (cells ^{per} L)$^{-1}$ day^{-1}. The blue curve shows the solution (17) for $P_o = 3000$ cells ^{per} mL. (b) The curves display the solutions (20) for $P_o = 2000$ cells ^{per} mL and $m = 2.5\times10^{-7}$ (cells ^{per} mL)$^{-1}$ day^{-1} for (red dashed curve) $g_r = 0$, (black curve) $g_r = 0.25$ day^{-1}, and (blue curve) $g_r = 0.51$ day^{-1}.

Algae growth is no longer unlimited in this solution. Instead, P adjusts to a positive equilibrium value of $P_\infty = \mu/m$ (**Figure 4a**). This equilibrium value varies subject to environmental factors influencing μ and m. Dependent on the initial value P_o, this transient adjustment can be either an increase or a decrease of P. A typical value of $\gamma = 432$ day^{-1} (=

0.005 s^{-1}) corresponds to $m = 2.5\times10^{-7}$ (cells ^{per} L)$^{-1}$. The corresponding equilibrium value for $\mu = 0.5$ day^{-1} is $P_\infty = \mu/m = 2\times10^6$ cells ^{per} L (= 2×10^3 cells ^{per} mL).

The timescale associated with (17) is derived as follows. Firstly, (17) can be elegantly rewritten in reciprocal form as:

$$1/P = 1/P_\infty + \left(1/P_o - 1/P_\infty\right)\exp(-\mu t) \text{ with } P_\infty = \mu/m \quad (18)$$

Defining a target value by $1/P_o - 1/P = 1/P_{target}$, then the timescale t^* to reach this target value follows from:

$$t^* = \mu^{-1}\ln\left(P_{target}/P^*\right) \text{ where } P^* = \left(1/P_o - 1/P_\infty\right)^{-1} \quad (19)$$

It follows that the timescale t^* depends on all parameters in (17). For example, $\mu = 0.5$ day^{-1}, $P_o = 1$ cell ^{per} mL, $P_\infty = 1000$ cells ^{per} mL, and a target value of $P_{target} = 0.9\ P_\infty$, correspond to a timescale of $t^* = 18.9$ days, which agrees well with the curve displayed in Figure 4a.

Given that the grazing term is formulated as an offset of the growth term, the solution of the full equation (1) without physical effects is simply given by:

$$P(t) = \mu^*[m + \kappa\exp(-\mu^* t)]^{-1} \text{ with } \kappa = \mu^*/P_o - m \quad (20)$$

which is the same as (16) but with $\mu^*=\mu-g_r$. If $\mu^* > 0$, the solution converges towards an equilibrium value of $P(t=\infty) = \mu^*/m$. Conversely, if $\mu^* < 0$, P asymptotically decreases to zero (**Figure 4b**). This solution illustrates that, in addition to physical dilution, zooplankton grazing pressure contributes significantly to the dissipation of *K. mokimotoi* blooms in the sea.

The following consideration explores the seasonal variation of the simulated *K. mokimotoi* growth based on the seasonal temperature cycle; that is,

$$T(month) = 18^oC + 6^oC\cos[2\pi(month - 1)/12] \quad (21)$$

where *month* is the month number, which is characteristic of South Australian gulfs. Using (5) with a constant salinity of $S = 36$ ppt is then used to calculate $P_\infty = \max(\mu^*/m, 0)$ for different values of g_r. With $\alpha = 1$ in (11), the seasonal cycle of P_∞ attains a minimum during the period June to August (**Figure 5a**). With inclusion of zooplankton grazing at a rate of 0.2

284 day^{-1}, the values of P_∞ fall to zero during this 3-month period which allows the *K. mokimotoi*
285 bloom to dissipate. On the other hand, the results are markedly different with use of a
286 temperature-dependent mortality rate based on (13). Then, the temperature effect induces
287 dramatic transient increases of P_∞ around May and September (**Figure 5b**) caused by a
288 disproportional decrease in m. This feature can lead to sudden unrealistic growth spurts of the
289 toxic algae the simulations. Hence, it is advised not to use (13) in *K. mokimotoi* models.

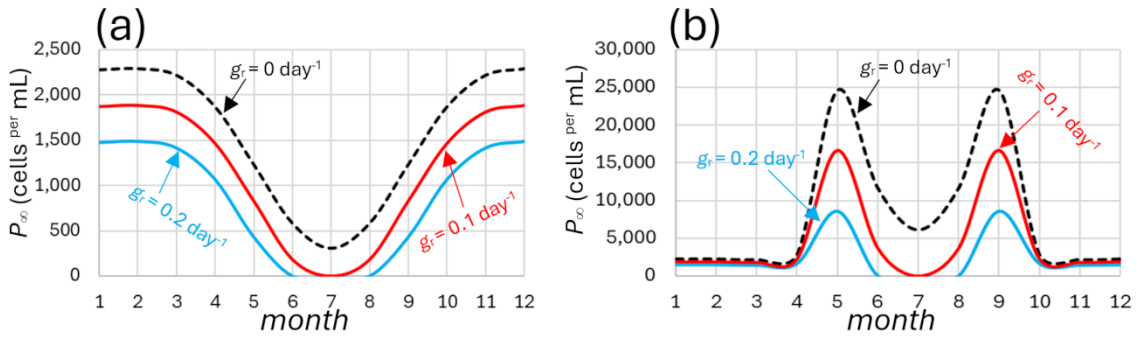

290

291 **Figure 5:** Equilibrium value $P_\infty = \max(\mu^*/m, 0)$ (cells ^{per} mL) for different grazing rates g_r
292 for $\mu = 0.5$ day^{-1}, $\gamma = 432$ day^{-1} and $m_o = 5\times10^{-5}$ (cells ^{per} mL)$^{-1}$ for (a) $\alpha = 1$ and b) α given by
293 (13) in equation (11).

294 2.3. Experimental design

295 Using spatially uniform temperature and salinity values as initial conditions, the
296 hydrodynamic model is first executed without biological effects until the establishment of
297 robust climatological seasonal cycles of temperature and salinity distributions, which takes
298 ~3-4 years of simulation. The model simulation is then continued for another 2 years (using
299 the same model forcing) with the inclusion of the *K. mikimotoi* model. The algae is hereby
300 released with a concentration of $P_o = 1000$ cells ^{per} mL (= 1,000,000 cells ^{per} L) in coastal
301 waters along the southern headland of the Fleurieu Peninsula, displayed by the yellow
302 rectangle in Figure 1. The release date is the 1 March 2025. For comparison, a passive
303 Eulerian tracer C is released with the same initial concentration in the same region without
304 any biological growth. This additional tracer study helps to understand the physical dispersal
305 characteristics of the study region.

306

307

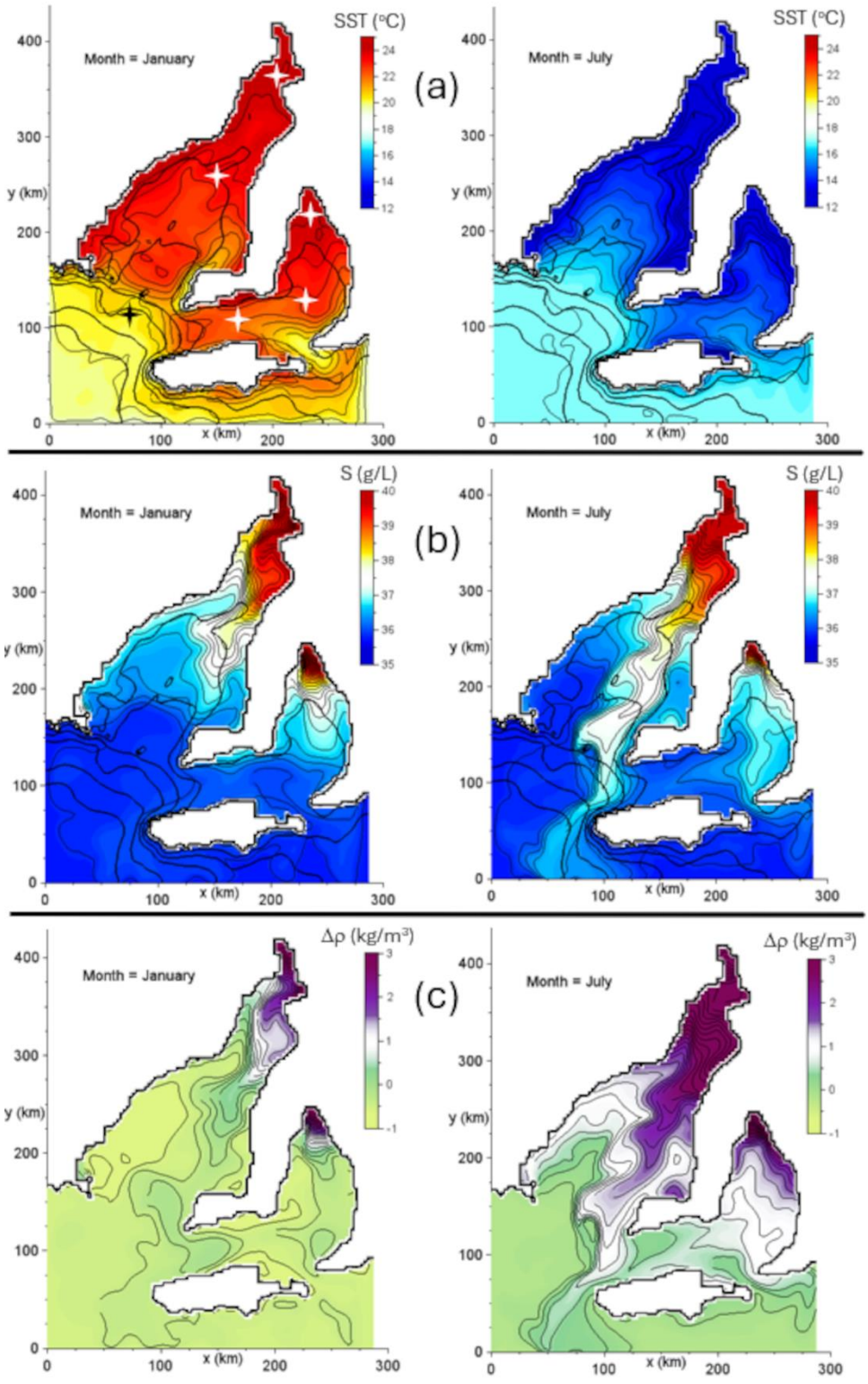

Figure 6: Horizontal distributions (color shading and thin lines) for (left panels) January and (right panels) July of a) sea surface temperature SST (°C) (CI = 0.5°C), b) near-bottom salinity (ppt) (CI = 0.2 ppt), and c) near-bottom density excess $\Delta\rho$ (kg/m^3) relative to ρ_o = 1026 (kg/m^3) (CI = 0.2 kg/m^3). Thick lines are bathymetric contours (CI = 20 m). The stars in panel (a) show locations featured in Figure 7.

3. Results and Discussion

3.1 Physical Features

The temperature of gulf water varies seasonally by ΔT = 8-10°C due to the surface heat-flux cycle (**Figure 6a**). Despite this pronounced seasonal cycle, horizontal temperature gradients are generally relatively small (<1°C) except near the entrances to the gulfs. Strong tidal flows in Backstairs Passage generate a tidal mixing zone where slightly colder surface water appears during austral summer months. In contrast, the salinity distribution displays strong spatial gradients with differences >5 g/kg throughout the year, while experiencing less seasonal variations (**Figure 6b**). Hypersaline water with salinities >40 ppt is found in the upper reaches in both gulfs throughout the year, and a "tongue" of hypersaline water extends southward along the eastern side of the gulfs.

The gulf's circulation and the exchange circulation with ambient shelf water is primarily driven by horizontal density gradients. While such density-gradients gradients exist throughout the year, their magnitude varies seasonally significantly in the southern section of both gulfs (**Figure 6c**). Summertime atmospheric warming of the water column compensates for salinity effects on seawater density and horizontal density gradients are markedly reduced (Figure 6c left panel). In stark contrast, wintertime atmospheric cooling of the hypersaline water induces a density excess of >2 kg/m^3 which generates a pronounced density-driven outflow from Spencer Gulf (Figure 6c right panel). A smaller density excess of ~1 kg/m^3 generates two weaker outflow branches in Gulf St. Vincent. One branch extends westward across Investigator Strait to join the outflow from Spencer Gulf. The other branch is an outflow through Backstairs passage. Due to volume conservation, the outflow draws in ambient shelf water during winter months. This leads to clockwise circulation patterns in both gulfs (Kämpf et al., 2010).

Figure 7 displays the simulated climatological seasonal cycles of depth-averaged temperature and salinity values for selected regions in both Spencer Gulf and Gulf St. Vincent at the locations shown in Figure 6a. Due to the shallow-water effect, the seasonal temperature cycle is amplified compared with the ambient shelf water. The seasonal salinity cycle is controlled by the seasonally varying inflow of ambient shelf water that makes up for the salinity increases due to evaporation. Due to sheer size of the gulfs, their upper reaches remain hypersaline throughout the year with salinities exceeding 40 ppt. This implies a slow

flushing of the gulfs with ambient shelf water with flushing times exceeding 1.5 years in upper Spencer Gulf (Kämpf et al., 2010).

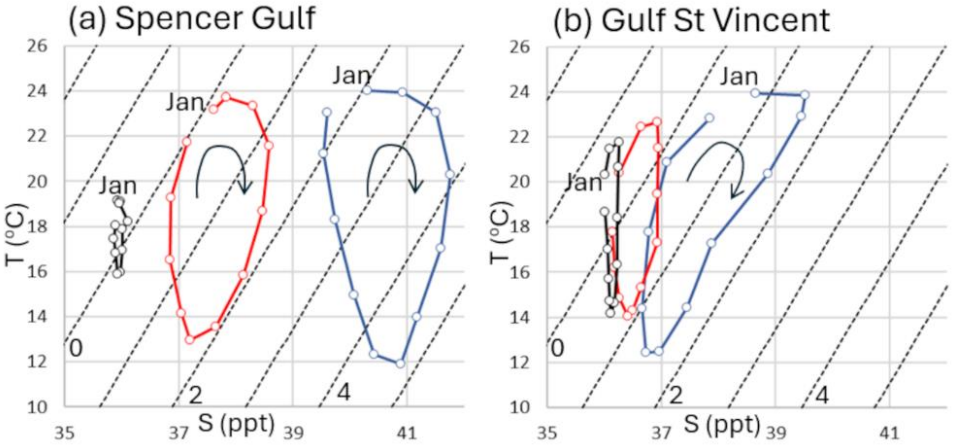

Figure 7: Temperature-salinity-time diagrams for the locations shown in Figure 6. Markers display monthly-mean data starting in January (marked as "Jan") and following the curves clockwise. Dashed lines are isopycnals (kg/m^3) relative to ρ_o = 1026 (kg/m^3) (CI = 1 kg/m^3).

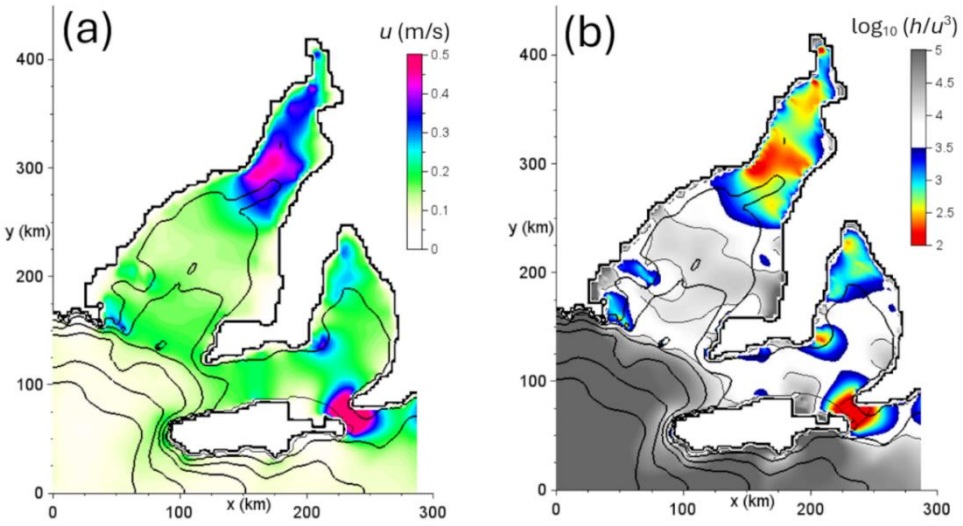

Figure 8: Horizontal distributions (color shading) of monthly averages of a) depth-averaged horizontal flow speed u (m/s), and b) the Simpson-Hunter parameter K = log10 (h/u^3), where h is total water depth. Values do not display interannual variability. Thick lines are bathymetric contours (CI = 20 m).

Tidal currents are the swiftest with monthly averaged speeds >0.4 m/s in both Backstairs Passage and the upper Spencer Gulf (**Figure 8a**). Is it obvious that the strong tidal flows across Backstairs Passage act as a transfer agent of floating substances, such as algae, between the waters of Gulf St. Vincent and the ambient coastal ocean.

Tidal mixing zones are often characterized by threshold values of the Simpson-Hunter parameter which is defined by (Simpson and Hunter, 1974):

$$K = \log_{10}(h/u^3) \quad (22)$$

where h is total water depth, and u is the vertically averaged characteristic horizontal speed of tidal currents. On the global scale, tidal mixing fronts can be characterized by threshold values of K within the range of 1.6-3.2 (Timko et al., 2019). Threshold values of $K < 2.5$ are only found in the upper Spencer Gulf, the upper reaches of Gulf St. Vincent, and Backstairs Passage (**Figure 8b**). On the other hand, the vertically averaged shear rate γ (11) is closely correlated with total water depth throughout the year (**Figure 9**). Is has a value of $\gamma \approx 0.01$ s^{-1} closer to the shore and values of ~0.004-0.006 s^{-1} elsewhere in the gulfs.

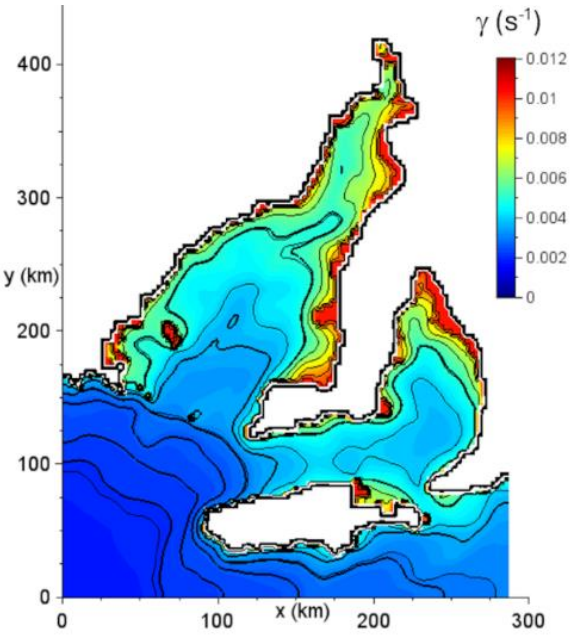

Figure 9: Horizontal distributions (color shading and thin lines; CI = 0.01 s^{-1}) of the monthly average of depth-averaged shear rate γ (s^{-1}). Values do not display significant interannual variability. Thick lines are bathymetric contours (CI = 20 m).

3.2 Dispersal Characteristics

Figure 10 displays the dispersal of a passive Eulerian tracer C (cells per ml) that is instantly released on 1 March 2025 with a concentration of 1,000 cells ^{per} mL throughout the water column in the yellow rectangle shown in Figure 1. Within two months of integration (March-April), this tracer appears highly diluted with a concentration of 20-25 cells ^{per} mL in the region where the lower Gulf St. Vincent joins the Investigator Strait (**Figure 10a**). Strong tidal currents in Backstairs Passage are responsible for both the appearance of the tracer in

the gulf and its strong dilution. In the following two months (May-June), being further diluted, the tracer is sheared diagonally across Investigator Strait and moved northward along the western side of Gulf St. Vincent (**Figure 10b**). This northward movement is a feature of the density-driven circulation in the gulf. During July-August, currents have fully dispersed the tracer patch in Investigator Strait, but a tracer patch with 5-10 cells ^{per} mL remains in the upper Gulf St. Vincent (**Figure 10c**), where it remains for the following 6 months (**Figure 10d-f**). This dispersal prediction for a passive tracer without biological effects indicates a dispersal pathway between the southern shelf of the Fleurieu Peninsula (where the *K. mikimotoi* bloom was first reported from) and upper reaches of Gulf St. Vincent on a timescale of 4 months.

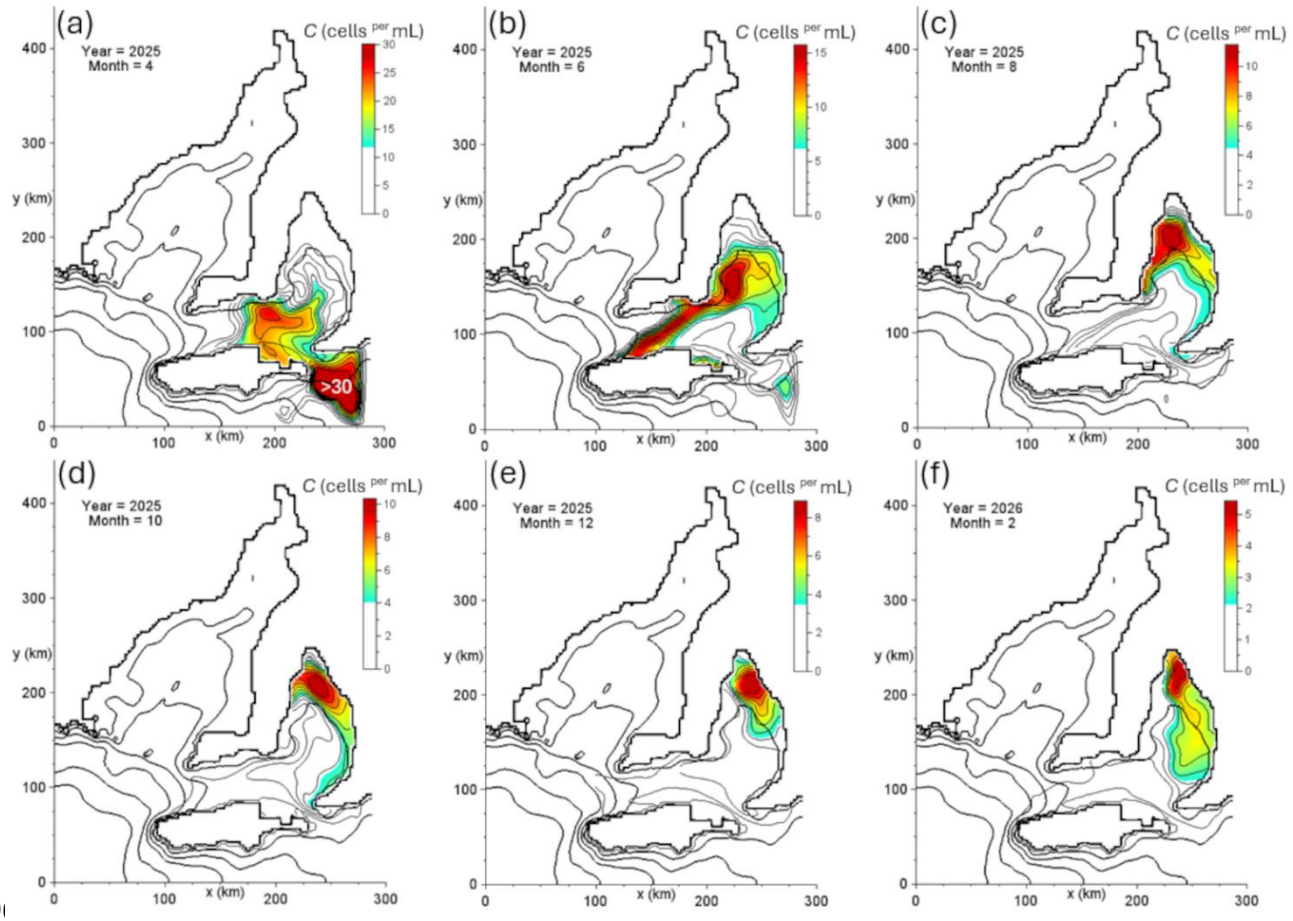

Figure 10: Surface distributions (color shading and thin lines) of monthly averages of a passive (no biology) Eulerian tracer *C* (cells ^{per} ml) that is instantly released on 1 March 2025 with a concentration of 1,000 cells ^{per} ml in the yellow rectangle shown in Figure 1 for a) April 2025, b) June 2025, c) August 2025, d) October 2025, e) December 2025, and f) February 2026. Thick lines are bathymetric contours (CI = 20 m). The contour interval is a tenth of the total range displayed in the color bars.

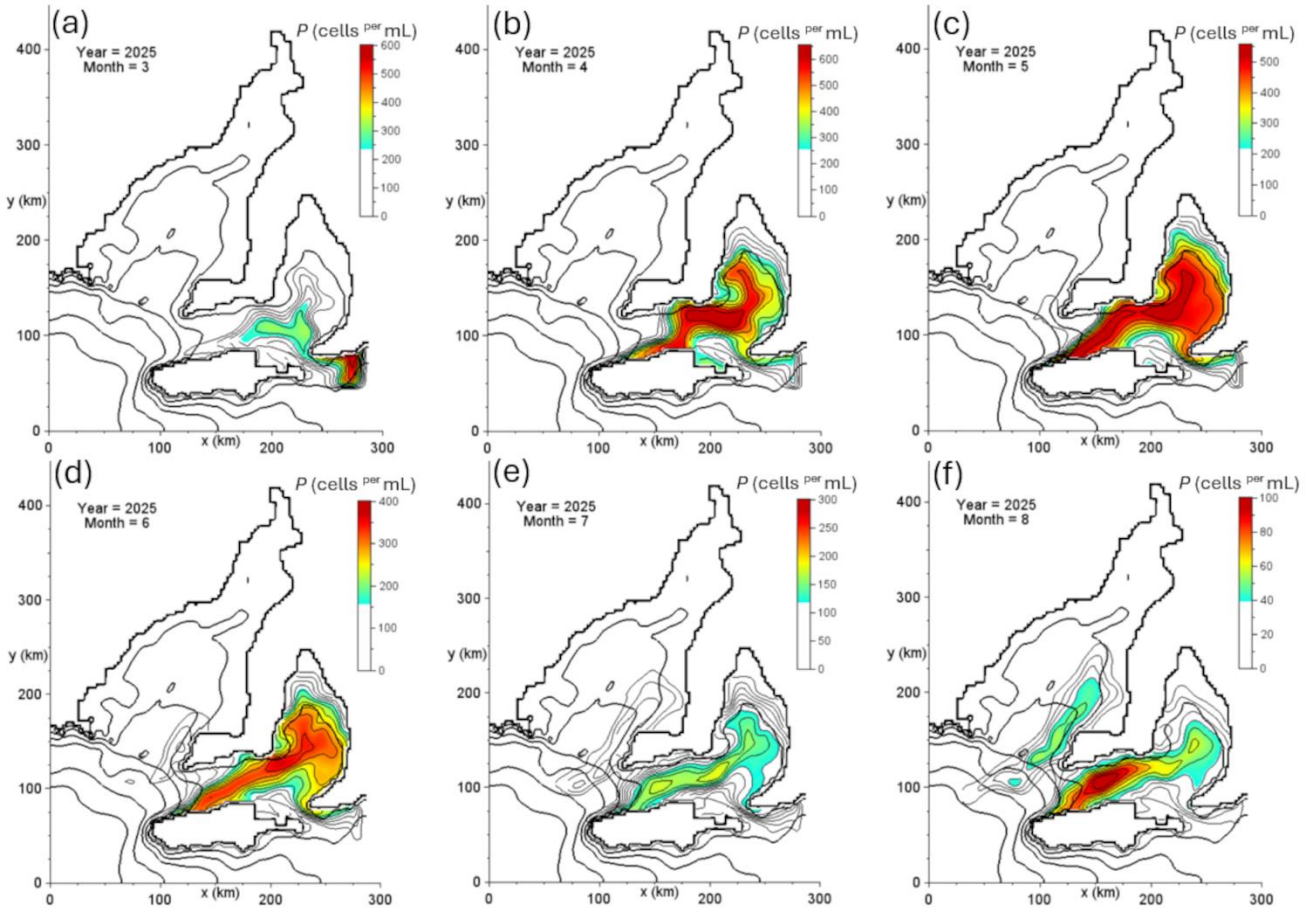

Figure 11: Model prediction. Surface distributions of monthly averages of *K. mikimotoi* concentrations (cells ^{per} mL) (color shading and think lines) with a zooplankton grazing rate of $g_r = 0.1$ day^{-1} shown every month from March 2025 to August 2025. Thick lines are bathymetric contours (CI = 20 m). The contour interval is a tenth of the total range displayed in the color bars.

3.3 Algae Bloom Predictions

In the first simulation scenario, the zooplankton grazing rate g_r is linearly increased from zero to a spatially uniform value of 0.1 day^{-1} within 30 days after the day of the model's algae initiation on 1. March 2025. Within a month, strong tides in Backstairs Passage have imported the algae to the lower Gulf St Vincent (**Figure 11a**). This is like the passive Eulerian tracer simulation (see Figure 10a), but due to biological growth the algae concentration has increased tenfold to 300 cells ^{per} mL. In April 2025, the algae concentration has increased to 600 cells ^{per} mL (**Figure 11b**). One branch of the bloom spreads westward into Investigator Strait along the northern coast of Kangaroo Island. Another branch of the bloom starts to spread northward along the western side of Gulf St. Vincent. Note that algae concentrations are lower here than shown in Figure 5a, which is mainly due to light limitation during nighttime. In May 202, the algae bloom extends over most of Investigator Strait and

the Gulf St. Vincent, except for the very upper reaches of the gulf (**Figure 11c**). In the following 3 months (June-August 2025), the algae bloom slowly dissipates in the Gulf St. Vincent to concentrations <60 cells ^{per} mL (**Figure 11 d-f**), which due to the temperature effect on the growth rate. Nonetheless, algae concentrations >80 cells ^{per} mL still exist in Investigator Strait. Moreover, an algae bloom of similar concentrations has evolved in the southeastern lower Spencer Gulf (**Figure 11f**). This bloom evolved from an advective event in May that transports algae at relatively low concentrations ~60 cells ^{per} mL from the western Investigator Strait into the lower Spencer Gulf (**Figure 12**), where it remains for the remainder of the year.

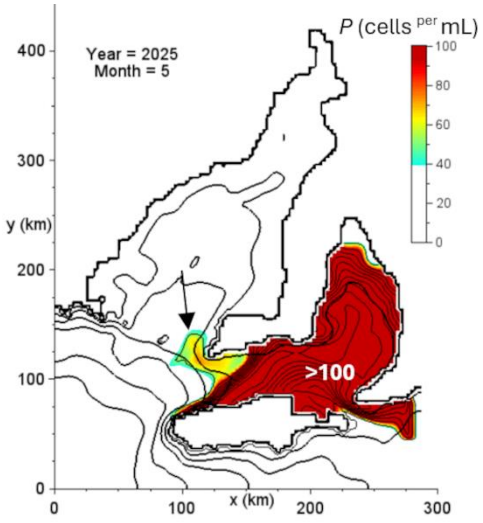

Figure 12: Model prediction. Same as Figure 11c but with a cutoff value of 100 cells ^{per} mL which reveals the event of algae transport into Spencer Gulf highlighted by the black arrow.

The increase in solar radiation during spring induces an enhancement in algae growth, and the algae concentration in the lower Spencer Gulf increases to 300 cells ^{per} mL in October 2025 in a circular path of 60 km in diameter (**Figure 13a**). There are also algae blooms outside the mouth of Spencer Gulf and along a tongue stretching along the northern coastline of Investigator Strait and into Gulf St. Vincent **(Figure 13b)**. Strong algae blooms with concentrations >600 cells ^{per} mL then evolve across a large portion of both gulfs and Investigator Strait throughout summer and autumn 2026 (**Figure 13c-d**) noting eastward leakage of algae-rich water through Backstairs Passage onto the Lacepede Shelf, again due to strong tidal stirring. While the algae bloom weakens in Gulf St. Vincent in winter 2026, it still retained relatively high concentrations >200 cells ^{per} mL in the lower Spencer Gulf (**Figure 13e-f**). Note that the upper reaches of the gulfs are largely devoid of algae, which comes from reduction of growth rates in hypersaline environments according to (5).

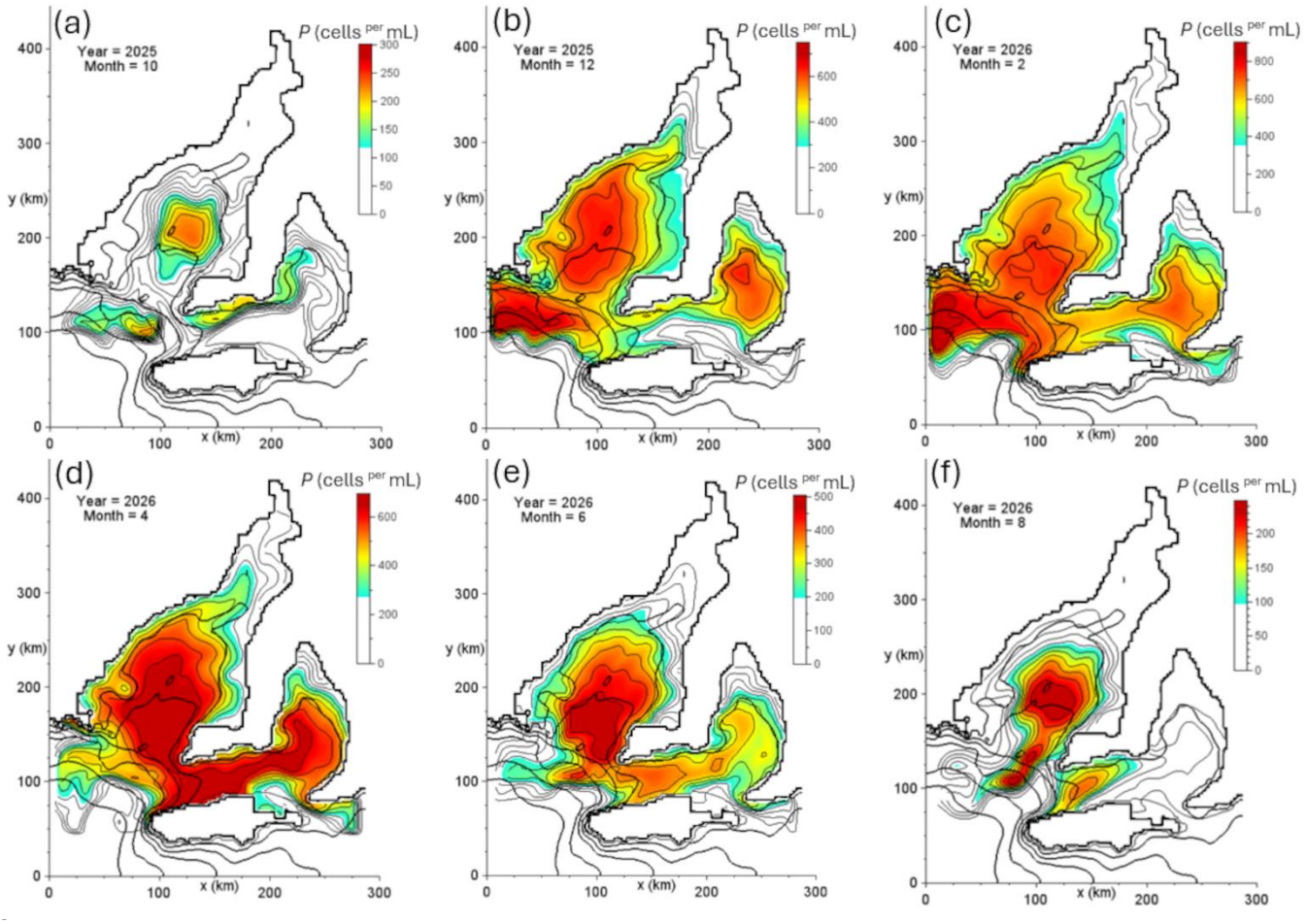

Figure 13: Model prediction. Same as Figure 11 but shown every two months from October 2025 to August 2026.

The situation is different for an increased zooplankton grazing rate of $g_r = 0.2$ day^{-1}, again linearly blended in during March 2025. While the initial development of the algae bloom in Gulf St. Vincent and Investigator Strait has a similar spatial structure as in the simulation with $g_r = 0.1$ day^{-1} (**Figure 14a-c**, compare with Figure 12a-c), its magnitude is markedly reduced. It only peaks at 200 cells per mL, which is threefold less compared with the first simulation. While this difference seems small, the algae concentration then continuous to fall to very low levels of 5 cells per mL in July 2025 and <0.1 cells per mL in August 2025 (**Figure 14d-f**). Thereafter it never recovers and algae concentration remain insignificantly small throughout 2026 not exceeding 0.2 cells per mL (**Figure 15a-f**). Moreover, significant algae blooms do not evolve in the Spencer Gulf throughout this simulation, but there is an indication of the existence of an algae patch (concentration <0.004 cells per mL) in the region in June (see Figure 15e).

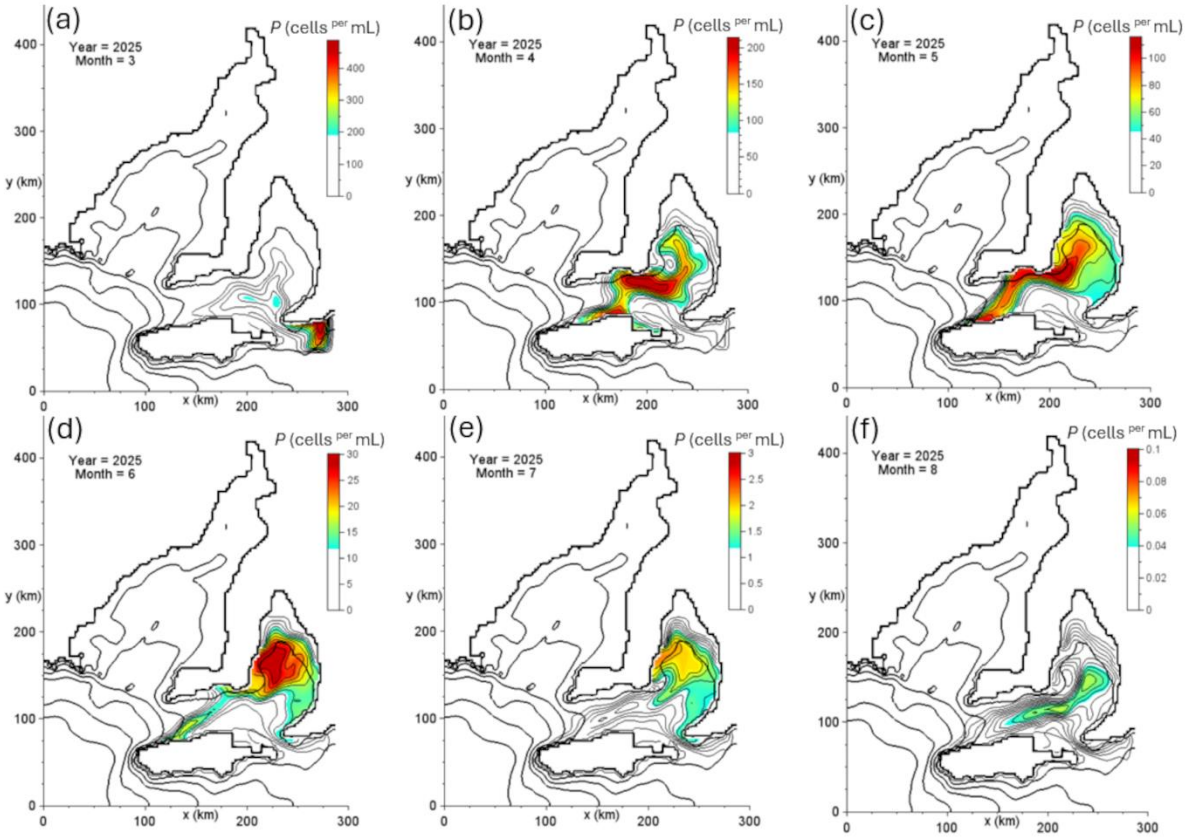

462

463 **Figure 14:** Model prediction. Same as Figure 11 but with $g_r = 0.2$ day^{-1}.

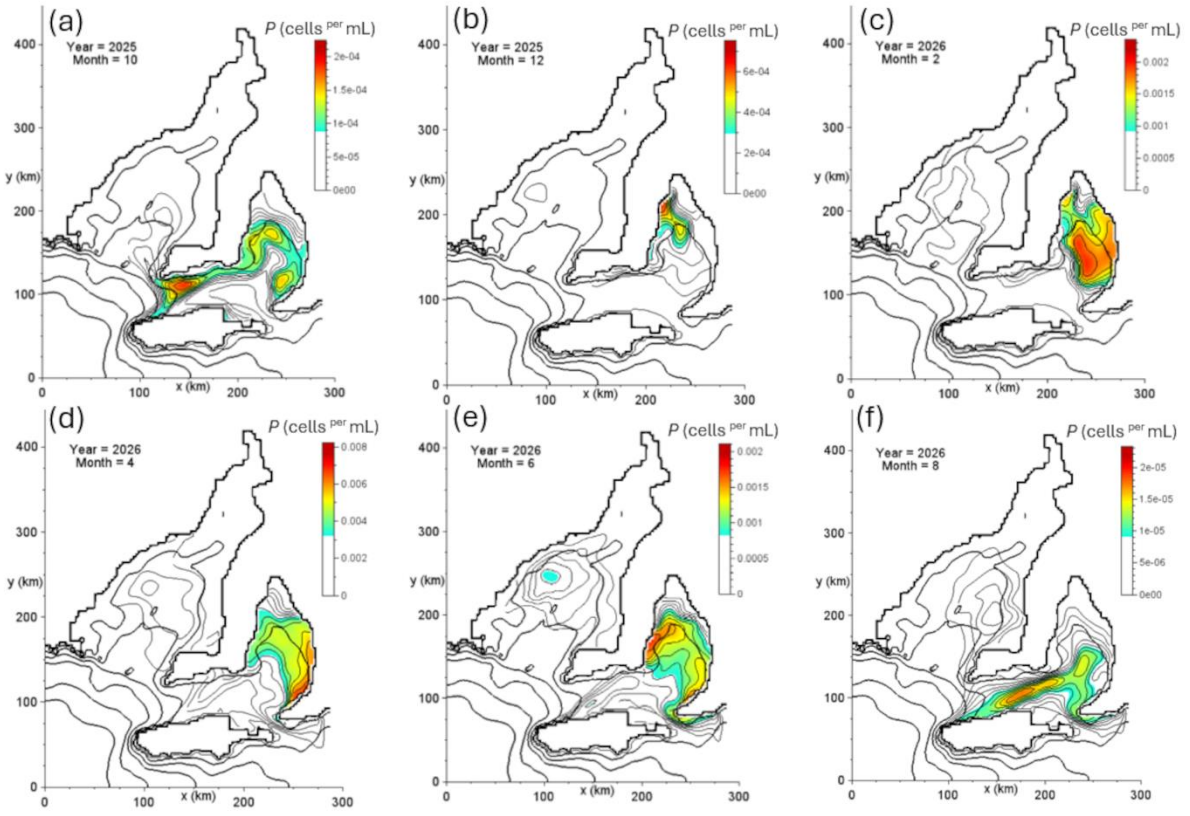

464

465 **Figure 15:** Model prediction. Same as Figure 13 but with $g_r = 0.2$ day^{-1}.

3.4 Final Discussion

In some regions, like the English Channel, *K. mikimotoi* blooms can be successfully detected with satellite-derived ocean colour data as a proxy for chlorophyll-*a* (chl-*a*) concentrations (Kurekin *et al.*, 2014). This is more difficult in shallow-water regions like South Australian Gulfs, where ocean colour data can be significantly biased due to interferences with the seafloor in optically shallow waters (<10-20 m), and suspended particles and coloured dissolved organic matter (CDOM) (Mélin, 2019; Staehr *et al.*, 2022).

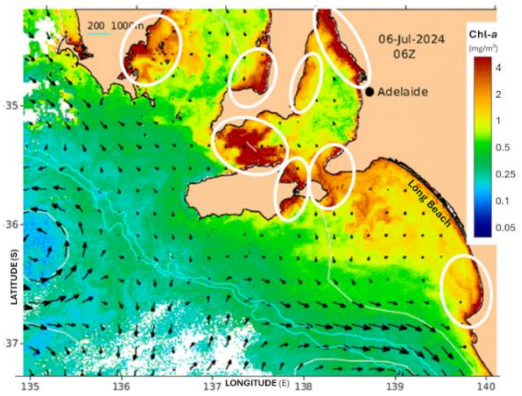

Figure 16. Satellite-derived chl-*a* distribution (mg/m^3) (color shading) for 6 July 2024 in the absence of any *K. mikimotoi* effects. White ellipses highlight regions of elevated levels. White areas are cloud biases, Cyan lines show the 200-m and 1000-m isobaths. Back arrows show altimeter-derived surface currents. Image source: Australia's Integrated Marine Observing System (IMOS) – IMOS is enabled by the National Collaborative Research Infrastructure Strategy (NCRIS). Maps are available at https://oceancurrent.aodn.org.au/.

The following discussion exclusively presents snapshot (not composites) of ocean-colour distributions that became available during days without cloud coverage. **Figure 16** shows a MODIS-Aqua chl-*a* distribution for early July 2024; that is, the winter preceding the *K. mikimotoi* bloom. As can be seen from the image, there are many areas of high values >2 mg/m^3, particularly around Backstairs Passage, Investigator Strait, upper Gulf St. Vincent, and on either side of the lower Spencer Gulf. While some of these areas may be real phytoplankton blooms triggered by wintertime recycling of nitrogen via seabed erosion (Kämpf and Kavi, 2017), others may be fake blooms such as the one in the northern shallows of Gulf St. Vincent. Note that the phytoplankton blooms on the Lacepede Shelf due to seasonal coastal upwelling are confined to the period November-April (Kämpf, 2025b).

Figure 17 shows a sequence of satellite chl-*a* distributions for the period from 21 March to 9 July 2025. In late March 2025, high chl-*a* values are found along the southern coastline of the Fleurieu Peninsula (where the *K. mikimotoi* bloom was first detected) (**Figure 17a**).

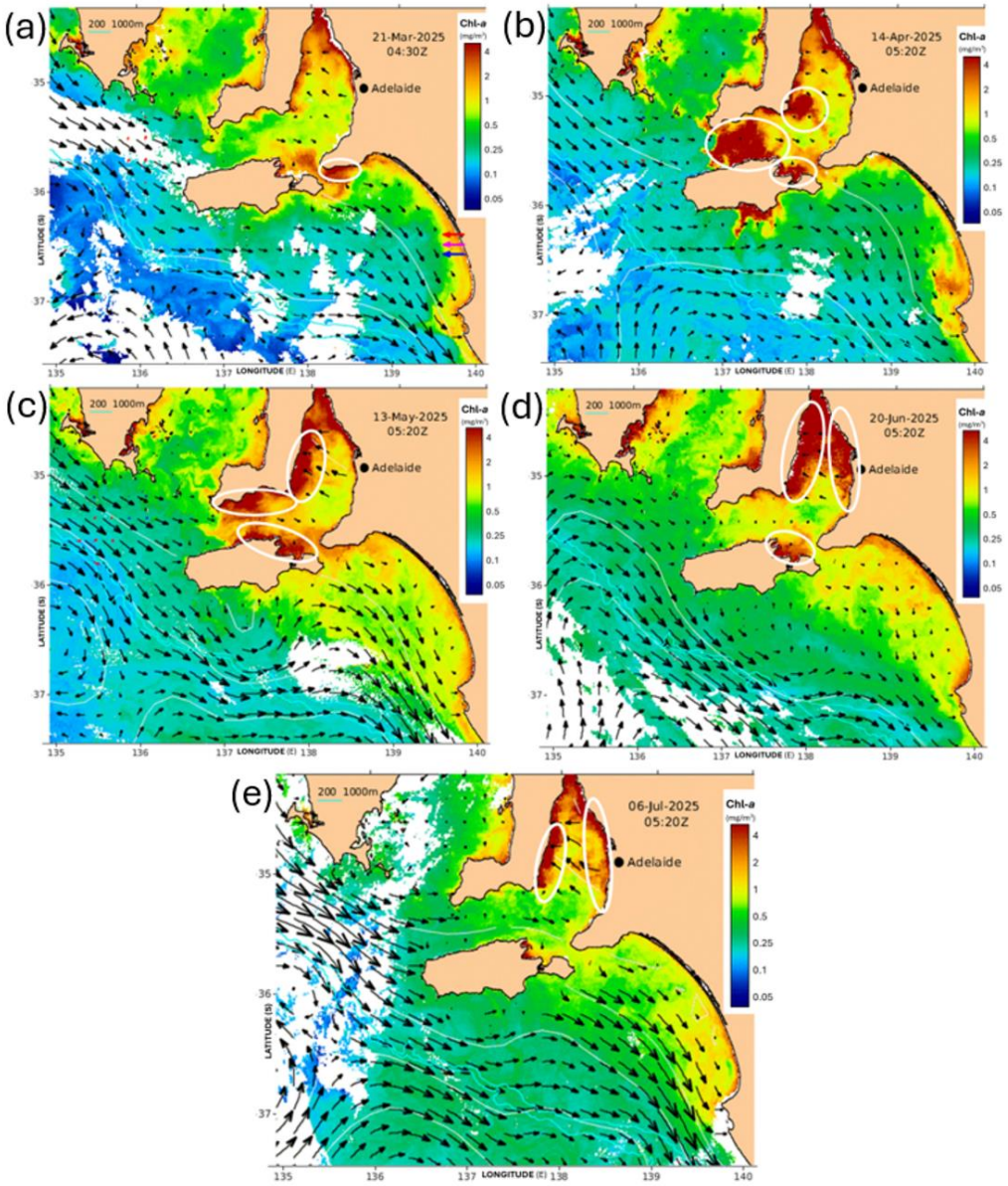

Figure 17. Satellite-derived chlorophyll-*a* distribution (mg/m^3) (color shading) for a) 21 March 2025, b) 14 April 2025, c) 13 May 2025, d) 20 June 2025, and e) 6 July 2025. White ellipses highlight high-value regions that could relate to *K. mikimotoi* effects. White areas are cloud biases. Cyan lines show the 200-m and 1000-m isobaths. Back arrows show altimeter-derived surface currents (which not accurate inside the gulfs). Image source: Australia's Integrated Marine Observing System (IMOS) – IMOS is enabled by the National Collaborative Research Infrastructure Strategy (NCRIS). Maps are available at https://oceancurrent.aodn.org.au/.

There are also high chl-*a* values in a region across Backstairs Passage that may not be related to this bloom. Other regions of elevated satellite chl-*a* levels, such as that in the upper Gulf St. Vincent, are not yet affected by the topic algae bloom. From mid-April to mid-May 2025, areas of high chl-*a* have evolved across Backstairs Passage and in near the southeastern corner of the Yorke Peninsula (**Figure 17b-c**), likely related to the spreading of the *K. mikimotoi* bloom. The satellite-derived chl-*a* distributions strongly resemble the simulated *K. mikimotoi* distribution (see Figures 11b-c and 14b-c). Interestingly, the satellite data for June and July 2025 suggest a weakening of the *K. mikimotoi* bloom in Investigator Strait (**Figure 17d-e**), presuming that the satellite signal is caused by the *K. mikimotoi* bloom, but bloom effects may still be present along the western and eastern sides of Gulf St. Vincent.

The onset of the *K. mikimotoi* bloom during March-May 2025 inferred from satellite data resembles more the simulation results with $g_r = 0.1$ day^{-1} (Figure 11b-c) while the bloom decay phase in Investigator Strait during May-June 2025 is more like the simulation with $g_r = 0.2$ day^{-1}. From the satellite data is May 2025 there is an indication of the possibility of algae leakage into lower Spencer Gulf (see Figure 17c), like the simulation result with $g_r = 0.1$ day^{-1} (see Figure 12).

4. Summary and Conclusion

The study applies a coupled physical-biological model to simulate the spreading of an unprecedented *K. mikimotoi* bloom in South Australian gulfs. In the absence of more accurate information, the model assumed a constant zooplankton grazing rate. Irresponsibly of this rate, the model simulations agree with reported timeline of the initial bloom spreading from its origination outside Backstairs Passage to the initial spreading first across Investigator Strait and later across the wider Gulf of St Vincent on a timescale of 2-3 months. This development and spreading of the bloom is not significantly affected by temperature, given that the algae growth is relative insensitive to temperature variations of 17.5–22.5°C (see Figure 3). Hence, climate-change effects are likely irrelevant for the initiation of the algae bloom. Causes of the onset of the algae bloom are unknown, but most likely related to bio-invasion.

The results presented strongly depend on the magnitude of zooplankton grazing (which is unknown). With a higher grazing rate of $g_r = 0.2$ day^{-1}, the model simulation predicted only a weaker algae bloom in Investigator Strait and Gulf St. Vincent that soon

534 dissipated without reappearance in the following summer. In stark contrast, a reduced grazing
535 rate of $g_r = 0.1$ day^{-1} produced a stronger algae bloom that leaked into Spencer Gulf to form
536 significant algae blooms in both gulfs in the following summer. Neither scenario can be ruled
537 out, given the lack of knowledge about zooplankton grazing rates associated with *K.*
538 *mikimotoi.* Further research is required to quantify zooplankton grazing rates.

539 Due to a reduced growth rate in hypersaline environments, the simulated *K. mikimotoi*
540 bloom did not spread into the upper reaches of gulfs, which could have devastating effects on
541 the Giant Australian Cuttlefish population in the upper Spencer Gulf. More laboratory
542 experiments are required to confirm this salinity effect on the growth rate of *K. mikimotoi*.

543 Due to existing biases and other types of phytoplankton blooms, satellite data of
544 chlorophyll-*a* on their own are not sufficient to derive the extent of spreading of *K. mikimotoi*
545 in South Australian gulfs. Satellite chl-*a* images should also not be used to inform the public
546 about the algae bloom spreading given the common alarming red areas many of which are not
547 associated with the *K. mikimotoi* bloom. Instead, extensive analyses of *in-situ* water samples
548 across both gulfs and Investigator Strait are required to monitor the possible reactivation of
549 the algae bloom in the future. This analysis is also essential for the improvement of coupled
550 physical-biological HAB prediction models, like the one used in this work.

551

552 **Acknowledgements:** This study did not receive external research support. Model simulations
553 were run on a standard laptop computer using the GFORTRAN compiler. Scilab
554 (https://www.scilab.org/) was used to prepare most graphs of this paper. Figure 1 uses
555 bathymetry data from Geoscience Australia. Figures 16 and 17 are based on maps sourced
556 from Australia's Integrated Marine Observing System (IMOS), which is enabled by the
557 National Collaborative Research Infrastructure Strategy (NCRIS). Maps are available at
558 https://oceancurrent.aodn.org.au/.

559 **Declarations:**

560 • The author has not made any use of AI technology in this research, neither in the
561 generation of the results nor in the writing of the text.
562 • This work has not received any funding from external sources.
563 • This work has not been published before and is not considered for publication
564 elsewhere.

References

Daw, M., 2025. Toxic algae found along coast. Yorke Peninsula Country Times 15 April 2025, https://arr.news/2025/04/15/toxic-algae-found-along-coast/ (last accessed 17 July 2025)

Dupavillon, J.L., Gillanders, B.M., 2009. Impacts of seawater desalination on the giant Australian cuttlefish *Sepia apama* in the upper Spencer Gulf, South Australia. *Mar. Environ. Res*. 67, 207–218. https://doi.org/10.1016/j.marenvres.2009.02.002

EPA, 2025. Harmful algal blooms (HABs) and marine heat waves. Information provided by the Environment Protection Authority of South Australia. https://www.epa.sa.gov.au/environmental_info/water_quality/harmful-algal-blooms#:~:text=Extensive%20monitoring%20has%20demonstrated%20that,around%20Waitpinga%20and%20Parsons%20beaches (last accessed 17 July 2025)

Furuya, K., Iwataki, M., Lim, P.T., Lu, S., Leaw, C.-P., Azanza, R.V., Kim, H.-G., Fukuyo, Y., 2018. Overview of harmful algal blooms in Asia. In: Glibert, P.M., Berdalet, E., Burford, M.A., Pitcher, G.C., Zhou, M. (Eds.) Global Ecology and Oceanography of Harmful Algal Blooms. Springer International Publishing, Cham, pp. 289–308.

Gaut, A.C., 2001. Pilchard (*Sardinops sagax*) mortality events in Australia and related world events. FRDC Project No. 99/227. 167pp. https://www.frdc.com.au/sites/default/files/products/1999-227-DLD.pdf (last accessed 17 July 2025)

Glibert, P.M., Pitcher, G., 2001. Global Ecology and Oceanography of Harmful Algal Blooms: Science Plan: an International Programme Sponsored by the Scientific Committee on Oceanic Research (Scor) and the Intergovernmental Oceanographic Commission (Unesco) Scientific Committee on Oceanic Research; Intergovernmental Oceanographic Commission, Baltimore, MD Paris.

Glibert, P.M., Berdalet, E., Burford, M.A., Pitcher, G.C., Zhou, M., 2018. Harmful Algal Blooms and the Importance of Understanding Their Ecology and Oceanography. Ecological Studies. Springer International Publishing. http://doi.org/10.1007/978-3-319-70069-4_2

Government of South Australia (2025) Environment SA News SA harmful algal bloom update 08 July 2025 https://www.environment.sa.gov.au/news-hub/news/articles/2025/07/sa-harmful-algal-bloom-update (last accessed 17 July 2025)

Gentien, P., Lunven, M., Lazure, P., Youenou, A., Crassous, M.P., 2007. Motility and autotoxicty in Karenia mikimotoi (Dinophyceae). *Philos. Trans. R. Soc. B* 362 (1487), 1937–1946. http://doi.org/10.1098/rstb.2007.2079

Gillibrand PA, Siemering B, Miller PI, Davidson K., 2016. Individual-based modelling of the development and transport of a Karenia mikimotoi bloom on the North-west European continental shelf. *Harmful Algae* 118-134. http://doi.org/10.1016/j.hal.2015.11.011.

Kämpf, J., Doubell, M., Griffin, D., Matthews, R.L., Ward, T.M., 2004. Evidence of a large seasonal coastal upwelling system along the southern shelf of Australia. Geophys. Res. Lett. 31, L09310. https://doi.org/10.1029/2003GL019221

Kämpf, J, Kavi, K., 2017. On the "hidden" phytoplankton blooms on Australia's southern shelves Geophysical Research Letters 44 (3), 1466-1473. https://doi.org/10.1002/2016GL072096

Kämpf, J., Brokensha, C., Bolton, T., 2009. Hindcasts of the fate of desalination brine in large inverse estuaries: Spencer Gulf and Gulf St. Vincent, South Australia. *Desalin. Water Treat.* 2(1-3), 335–344. https://doi.org/10.5004/dwt.2009.264

Kämpf, J., Payne, N., Malthouse, P., 2010. Marine connectivity in a large inverse estuary. *J. Coast. Res.* 26 (6), 1047–1056. https://doi.org/10.2112/JCOASTRES-D-10-00043.1

Kämpf, J., 2014. South Australia's large inverse estuaries: On the road to ruin. In E. Wolanski (Ed.) Estuaries of Australia in 2050 and beyond. Estuaries of the World. (pp. 153–166) Dordrecht, The Netherlands: Springer Science & Business Media. https://doi.org/10.1007/978-94-007-7019-5_9

Kämpf, J., Ellis, H., 2015. Hydrodynamics and flushing of Coffin Bay, South Australia: A small tidal inverse estuary of interconnected bays. *J. Coastal Res.* 31 (2), 447–456. https://doi.org/10.2112/JCOASTRES-D-14-00046.1

Kämpf, J., 2025a. On the upwelling-driven zonation of nitrogen, phytoplankton, and zooplankton in the eastern Great Australian Bight, Australia: A coupled physical-biological modelling study. *Oceanologia*, in press.

Kämpf, J., 2025b. Phytoplankton and zooplankton production in the Bonney Coast upwelling, Australia: A coupled physical-biological model investigation. *Cont. Shelf Research*, 285, 105373, https://doi.org/10.1016/j.csr.2024.105373

Kämpf, J., 2025c. The Coffin Bay Estuary: Influences from coastal upwelling in the eastern Great Australian Bight. Journal of Marine Systems. Accepted pending minor revisions.

KIC (2025) Kangaroo Island Council. Karenia mikimotoi Algal Bloom – Information for the Community. Published 9th May 2025 https://www.kangarooisland.sa.gov.au/notice-board/news-and-notices/latest-news/karenia-mikimotoi-algal-bloom-information-for-the-community (last accessed 17 July 2025)

Kurekin, A.A., Miller, P.I., Van der Woerd, H.J., 2014. Satellite discrimination of Karenia mikimotoi and Phaeocystis harmful algal blooms in European coastal waters: Merged classification of ocean colour data. *Harmful Algae* 31, 163-176, https://doi.org/10.1016/j.hal.2013.11.003

Lennon, G.W., Bowers, D.G., Nunes, R.A., Scott, B.D., Ali, M., Boyle, J., Wenju, C., Herzfeld, M., Johansson, G., Nield, S., Petrusevics, P., Stephanson, P., Suskin, A.A., Wijffels, S.E.A., 1987. Gravity currents and the release of salt from an inverse estuary. *Nature*, 327, 695–697. https://doi.org/10.1038/327695a0

Li, X., Yan, T., Yu, R., Zhou, M. (2019) A review of karenia mikimotoi: Bloom events, physiology, toxicity and toxic mechanism. *Harmful Algae* 90, 101702, https://doi.org/10.1016/j.hal.2019.101702.

Loyer S., 2001. Modélisation de la production phytoplanctonique dans la zone côtière atlantique enrichie par les apports fluviaux. Ph.D. thesis, Université de Paris VI, p. 256. Available at: https://archimer.ifremer.fr/doc/00000/3798/3329.pdf (last accessed on 17 July 2025)

Loyer, S., Lazure, P., Gentien, P., Ménesguen, A., (2001) Modelling of Gymnodinium mikimotoï blooms along the French Atlantic coast: geographical and vertical distributions. Hydroécologie Appliquée 13(1), https://doi.org/10.1051/hydro:2001006

Luyten, P.J., Jones, J.E., Proctor, R., Tabor, A., Tett, P., Wild-Allen, K., 1999. COHERENS - A Coupled Hydrodynamical-Ecological Model for Regional and Shelf Seas: User Documentation; MUMM Report; Management Unit of the North Sea: Brussels, Belgium, 914 pp., https://uol.de/f/5/inst/icbm/ag/physoz/download/from_emil/COHERENS/print/userguide.pdf (last accessed 17 July 2025)s

Mélin, F. (Ed.), 2019. Uncertainties in Ocean Colour Remote Sensing. IOCCG Report Series, No. 18, International Ocean Colour Coordinating Group, Dartmouth, Canada. http://dx.doi.org/10.25607/OBP696.

Middleton, J., Doubell, M., James, C., Luick, J., van Ruth, P., 2013. PIRSA Initiative II: carrying capacity of Spencer Gulf: hydrodynamic and biogeochemical measurement modelling and performance monitoring. Final Report for the Fisheries Research and Development Corporation. South Australian Research and Development Institute (Aquatic Sciences), Adelaide. SARDI Publication No. F2013/000311-1. SARDI Research Report Series No. 705. 97pp. https://www.frdc.com.au/sites/default/files/products/2009-046-DLD.pdf (last accessed 17 June 2025)

Moum J.N., Lueck R.G., 1985. Causes and implications of noise in oceanic dissipation measurements. *Deep-Sea Res*. 32, 379–392. https://doi.org/10.1016/0198-0149(85)90086-X

Nakamura, Y., Suzuki, S., Hiromi, J., 1996. Development and collapse of a Gymnodinium mikimotoi red tide in the Seto Inland Sea. *Aquat. Microb. Ecol.* 10 (2), 131–137. https://doi.org/10.3354/ame010131

Nakamura, Y., Suzuki, S.Y., Hiromi, J., 1995. Population dynamics of heterotrophic dinoflagellates during a Gymnodinium mikimotoi red tide in the Seto Inland Sea. *Mar. Ecol. Prog. Ser.* 125 (1-3), 269–277. http://www.jstor.org/stable/24854676

Nielsen, M.V., Tonseth, C.P., 1991. Temperature and salinity effect on growth and chemical composition of Gyrodinium aureolum Hulburt in culture. *J. Plankton Res.* 13 (2), 389–398. https://doi.org/10.1093/plankt/13.2.389

679 Richardson, B.J., 1982. Geographical distribution of electrophoretically detected protein
680 variation in Australian commercial fisheries. III Western king prawn, *Penaeus*
681 *latisulcatus Kishinouye*. *Austr. J. Mar. Freshw. Res.* 33, 933–937.
682 https://doi.org/10.1071/MF9820933

683 Roberts, S.D., Wilkinson, C., Stobart, B., Doubell, M., van Ruth, P., Gilliland, J., 2014. Fish
684 Kill Investigation: Coffin Bay harmful algal (Karenia mikimotoi) bloom February 2014.,
685 Primary Industries and Regions South Australia. PIRSA Fisheries Aquaculture Division
686 Adelaide. Available at:
687 https://www.researchgate.net/publication/263620467_Fish_Kill_investigation_Coffin_Ba
688 y_harmful_algal_bloom_February_2014 (last accessed 17 July 2025)

689 Simpson, J.H., Hunter, J.R., 1974. Fronts in the Irish Sea. *Nature, 250, 404–406.*
690 *https://doi.org/10.1038/250404a0*

691 Sournia, A., 1995. Red tide and toxic marine phytoplankton of the world ocean: an inquiry
692 into biodiversity. In Lassus, P. et al. (Eds.) Harmful marine algal blooms: Proceedings of
693 the Sixth International Conference on toxic marine phytoplankton, October 18-22, 1993,
694 103–112.Nantes, France.

695 Staehr, S.U., Van der Zande, D., Staehr, P.A.U., Markager, S., 2022. Suitability of
696 multisensory satellites for long-term chlorophyll assessment in coastal waters: A case
697 study in optically complex waters of the temperate region. *Ecol. Indic.* 134, 108479.
698 https://doi.org/10.1016/j.ecolind.2021.108479.

699 Timko, P.G., Arbic, B.K., Hyder, P., Richman, J.G., Zamudio, L., O'Dea, E., Wallcraft, A.J.,
700 Shriver, J.F., 2019. Assessment of shelf sea tides and tidal mixing fronts in a global ocean
701 model. *Ocean Modell.* 136, 66–84. https://doi.org/10.1016/j.ocemod.2019.02.008
702

Figure Captions

Figure 1: Bathymetry (m) of the model domain (color shading and lines; CI = 5 m; thick lines are shown with CI = 20 m). The Australia map shows the location of South Australia's gulfs. The yellow rectangle shows the algae release region. The red star shows the location of Waitpinga Beach where the toxic algae was first identified. Data source: Geoscience Australia.

Figure 2: Sea foam produced by the *K. mikimotoi* bloom at Waitpinga Beach on the southern headland of the Fleurieu Peninsula) in mid-March 2025. Image credit: Caroline Horn (ABC). Reproduced with permission.

Figure 3: Projections of the maximum growth rate μ_o under saturated light and nutrient conditions for (blue curve) a constant temperature of $T = 20^oC$ and (red curve) a constant salinity of $S = 35$ ppt, calculated from (5).

Figure 4: Analytical solutions for $\mu = 0.5$ day^{-1}. (a) The dashed black curve is the solution (15) for $P_o = 1$ cell ^{per} ml. The red curve is the corresponding solution (17) with $m = 7.5\times10^{-7}$ (cells ^{per} L)$^{-1}$ day^{-1}. The blue curve shows the solution (17) for $P_o = 3000$ cells ^{per} mL. (b) The curves display the solutions (20) for $P_o = 2000$ cells ^{per} mL and $m = 2.5\times10^{-7}$ (cells ^{per} mL)$^{-1}$ day^{-1} for (red dashed curve) $g_r = 0$, (black curve) $g_r = 0.25$ day^{-1}, and (blue curve) $g_r = 0.51$ day^{-1}.

Figure 5: Equilibrium value $P_\infty = \max(\mu^*/m, 0)$ (cells ^{per} mL) for different grazing rates g_r for $\mu = 0.5$ day^{-1}, $\gamma = 432$ day^{-1} and $m_o = 5\times10^{-5}$ (cells ^{per} mL)$^{-1}$ for (a) $\alpha = 1$ and b) α given by (13) in equation (11).

Figure 6: Horizontal distributions (color shading and thin lines) for (left panels) January and (right panels) July of a) sea surface temperature SST (^oC) (CI = 0.5^oC), b) near-bottom salinity (ppt) (CI = 0.2 ppt), and c) near-bottom density excess $\Delta\rho$ (kg/m^3) relative to ρ_o = 1026 (kg/m^3) (CI = 0.2 kg/m^3). Thick lines are bathymetric contours (CI = 20 m). The stars in panel (a) show locations featured in Figure 7.

Figure 7: Temperature-salinity-time diagrams for the locations shown in Figure 6. Markers display monthly-mean data starting in January (marked as "Jan") and following the curves clockwise. Dashed lines are isopycnals (kg/m^3) relative to ρ_o = 1026 (kg/m^3) (CI = 1 kg/m^3).

Figure 8: Horizontal distributions (color shading) of monthly averages of a) depth-averaged horizontal flow speed u (m/s), and b) the Simpson-Hunter parameter K = log10 (h/u^3), where h is total water depth. Values do not display interannual variability. Thick lines are bathymetric contours (CI = 20 m).

Figure 9: Horizontal distributions (color shading and thin lines; CI = 0.01 s^{-1}) of the monthly average of depth-averaged shear rate γ (s^{-1}). Values do not display significant interannual variability. Thick lines are bathymetric contours (CI = 20 m).

Figure 10: Surface distributions (color shading and thin lines) of monthly averages of a passive (no biology) Eulerian tracer *C* (cells ^{per} ml) that is instantly released on 1 March 2025 with a concentration of 1,000 cells ^{per} ml in the yellow rectangle shown in Figure 1 for a) April 2025, b) June 2025, c) August 2025, d) October 2025, e) December 2025, and f) February 2026. Thick lines are bathymetric contours (CI = 20 m). The contour interval is a tenth of the total range displayed in the color bars.

Figure 11: Model prediction. Surface distributions of monthly averages of *K. mikimotoi* concentrations (cells ^{per} mL) (color shading and think lines) with a zooplankton grazing rate of $g_r = 0.1$ day^{-1} shown every month from March 2025 to August 2025. Thick lines are bathymetric contours (CI = 20 m). The contour interval is a tenth of the total range displayed in the color bars.

Figure 12: Model prediction. Same as Figure 11c but with a cutoff value of 100 cells ^{per} mL which reveals the event of algae transport into Spencer Gulf highlighted by the black arrow.

Figure 13: Model prediction. Same as Figure 11 but shown every two months from October 2025 to August 2026.

Figure 14: Model prediction. Same as Figure 11 but with $g_r = 0.2$ day^{-1}.

Figure 15: Model prediction. Same as Figure 13 but with $g_r = 0.2$ day^{-1}.

Figure 16. Satellite-derived chl-*a* distribution (mg/m^3) (color shading) for 6 July 2024 in the absence of any *K. mikimotoi* effects. White ellipses highlight regions of elevated levels. White areas are cloud biases, Cyan lines show the 200-m and 1000-m isobaths. Back arrows show altimeter-derived surface currents. Image source: Australia's Integrated Marine Observing System (IMOS) – IMOS is enabled by the National Collaborative Research Infrastructure Strategy (NCRIS). Maps are available at https://oceancurrent.aodn.org.au/.

Figure 17. Satellite-derived chlorophyll-*a* distribution (mg/m^3) (color shading) for a) 21 March 2025, b) 14 April 2025, c) 13 May 2025, d) 20 June 2025, and e) 6 July 2025. White ellipses highlight high-value regions that could relate to *K. mikimotoi* effects. White areas are cloud biases. Cyan lines show the 200-m and 1000-m isobaths. Back arrows show altimeter-derived surface currents (which not accurate inside the gulfs). Image source: Australia's Integrated Marine Observing System (IMOS) – IMOS is enabled by the National Collaborative Research Infrastructure Strategy (NCRIS). Maps are available at https://oceancurrent.aodn.org.au/.